Galactic Rotation Curves from Full-Disk Newtonian Gravity: The Lost and Found Model

Adolfo Santa Fe Dueñas

Space Science Center, University of New Hampshire, Durham, NH 03824, USA

Email: adolfo.santafeduenas@my.utsa.edu

April 9, 2026

Abstract

The approximately flat outer parts of spiral galaxy rotation curves are commonly interpreted as evidence for a discrepancy between the observed baryonic mass and the dynamical mass inferred from the measured orbital velocities. In most standard analyses, this discrepancy is quantified using $v^2(R) = GM(< R)/R$, which is exact only under spherical symmetry. However, spiral galaxies are flattened disk systems, for which mass exterior to the galactocentric radius under consideration can contribute non-negligibly to the gravitational field.

We introduce the *Lost and Found* (LF) model, a geometrically consistent Newtonian framework based on direct full-disk gravitational integration and a parametrized representation of the disk surface density. In this approach, the gravitational field is computed without imposing spherical symmetry, and the disk mass distribution is represented by two exponential components with a smooth outer truncation.

We apply the LF model to a heterogeneous sample of disk galaxies spanning a broad range of masses and radial extents. The model reproduces the main observed features of the rotation curves, including the inner rise and the approximately flat outer behavior, without explicitly invoking a dark matter halo or modifying Newtonian gravity. Across the sample, the LF-inferred mass scales nearly linearly with the conventional dynamical mass, with a characteristic reduction factor $\eta_{\rm LF} \sim 0.67$.

These results indicate that part of the inferred mass discrepancy may arise from the geometric treatment of gravitation in disk galaxies, and motivate a reassessment of mass inference in non-spherical systems.

Also available on arXiv:2604.06917.

Keywords: galaxies: kinematics and dynamics – galaxies: structure – galaxies: spiral – dark matter – methods: numerical

1. Introduction

Since the mid-20th century, galactic rotation curves have played a central role in the study of mass distribution in galaxies. Observations of spiral systems, beginning with the pioneering work of Rubin et al. [1980], showed that the rotational velocity of stars and gas does not decline with radius as expected for a centrally concentrated or effectively enclosed mass distribution ($v \propto r^{-1/2}$), but instead remains approximately constant at large galactocentric distances.

This behavior has traditionally been interpreted as evidence for an additional, non-luminous mass component, commonly described in terms of dark matter halos [Navarro, 1996, Burkert, 1995]. Alternative approaches, most notably Modified Newtonian Dynamics (MOND), have instead proposed modifications to the law of gravity or inertia at low accelerations [Milgrom, 1983]. More recently, empirical relations such as the radial acceleration relation (RAR) have highlighted the close connection between the observed dynamics and the visible mass distribution [McGaugh et al., 2016].

Despite these different interpretations, many rotation-curve analyses share a common underlying step: the inference of gravitational acceleration from an assumed mass distribution. In many treatments, the circular velocity is estimated through the relation

$$v(r) = \sqrt{\frac{GM(< r)}{r}}, \tag{1}$$

where $M(< r)$ is interpreted as the mass enclosed within radius r. This expression is exact under spherical symmetry, where Newton's shell theorem applies [Binney and Tremaine, 2011]. Spiral galaxies, however, are not spherical systems, but flattened disk-like structures [Freeman, 1970].

For disk geometries, the gravitational contribution of material exterior to the galactocentric radius under consideration does not generally vanish.. Instead, the total acceleration must be obtained from the full mass

distribution of the disk [Casertano, 1983, Binney and Tremaine, 2011]. This raises the possibility that part of the inferred discrepancy between luminous and dynamical mass may depend not only on the amount of matter present, but also on how the gravitational field is geometrically evaluated.

Several previous studies have shown that Newtonian disk gravity can produce richer dynamical behavior than is captured by simplified enclosed-mass arguments [Casertano, 1983, Feng and Gallo, 2013, Ryan, 2013]. The present work revisits this issue by focusing specifically on the contribution of the full disk mass distribution, including material exterior to the radius of interest, and by quantifying the resulting impact on inferred galactic masses across a heterogeneous sample of spiral galaxies.

To this end, we introduce the *Lost and Found* (LF) model, a geometrically consistent Newtonian framework that combines direct full-disk gravitational integration with a two-component exponential representation of the disk surface density. This allows both the geometric contribution of the full disk and the radial structure of the mass distribution to be incorporated self-consistently, without imposing spherical symmetry. We show that this approach reproduces the main observed features of galactic rotation curves while systematically reducing the total mass required relative to conventional spherical-equivalent estimates.

The structure of this paper is as follows. Section 2 discusses the geometric limitations of the traditional enclosed-mass approach. Section 3 introduces the LF model and its mathematical formulation. Section 4 describes the numerical methodology. Section 5 presents the rotation-curve fits and mass comparisons. Section 6 discusses the physical interpretation and limitations of the model, and Section 7 summarizes the main conclusions.

2. Limitations of the Traditional Approach

2.1. Geometric Limitations of the Enclosed-Mass Approximation

A common first-order dynamical mass estimate in galactic rotation-curve studies is based on the expression:

$$v(r) = \sqrt{\frac{GM(r)}{r}}, \tag{2}$$

where $M(r)$ is assumed to be the mass enclosed within radius r. This formulation is widely used in galactic dynamics and is strictly valid under spherical symmetry, where Newton's shell theorem applies [Newton, 1687, Binney and Tremaine, 2011].

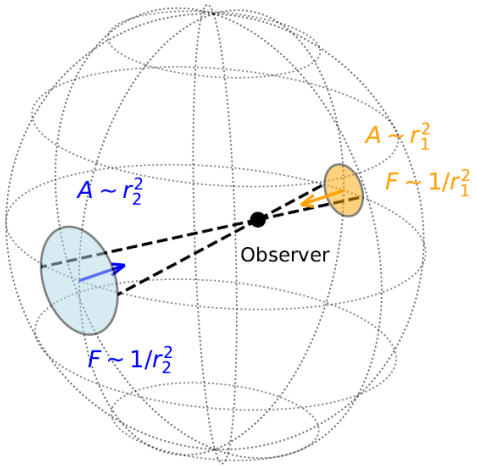

Figure 1: Gravitational force cancellation in a spherical shell. The projected area of distant mass elements increases as r^2, while the gravitational force decreases as $1/r^2$, leading to exact cancellation. This result depends critically on spherical symmetry. Adapted from Binney and Tremaine [2011].

Under spherical symmetry, the gravitational contribution from mass located outside the radius of interest cancels exactly, and only the enclosed mass determines the acceleration. This cancellation arises from the balance between the increase in projected area ($\propto r^2$) and the decrease in gravitational force ($\propto 1/r^2$), leading to a net zero contribution from spherical shells.

This cancellation mechanism is illustrated in Figure 1.

However, spiral galaxies are not spherically symmetric systems, but rather flattened, disk-like structures Freeman [1970]. In such geometries, the conditions required for exact cancellation are not satisfied.

As a result, mass elements located outside the radius of interest contribute non-negligibly to the total gravitational field [Freeman, 1970, Casertano, 1983, Binney and Tremaine, 2011]. Despite this, simplified interpretations of galactic rotation curves often invoke enclosed-mass or spherical-equivalent estimates even in disk systems, thereby neglecting contributions that are inherently present in flattened mass distributions [de Blok et al., 2008, Lelli et al., 2016].

2.2. Geometric Underestimation of Effective Mass

The use of the enclosed-mass approximation in disk systems leads to a geometric underestimation of the net gravitational contribution from the full mass distribution.

To illustrate this effect, consider a galactic disk of total radius R_{total} with uniform surface density. In the traditional approach, the gravitational field at a radius R_{obs} is computed by considering only the mass enclosed within that radius, corresponding to a circular region centered on the galactic nucleus:

$$A_{\text{trad}} = \pi R_{\text{obs}}^2. \tag{3}$$

All mass located at larger radii is neglected under the assumption that its contribution cancels.

In contrast, in a disk geometry, such cancellation does not occur globally. However, for the special case of constant surface density, one can construct a geometrically symmetric region centered on the observer whose contributions tend to cancel locally, providing an intuitive estimate of the portion of the disk that contributes most strongly to the net field. This region extends from the observer toward the nearest edge of the disk.

The remaining region can then be interpreted as the portion of the disk that contributes most directly to the net inward gravitational field in this simplified construction, forming a crescent-shaped (lune-like) region located opposite to the observer. This geometric difference is illustrated in Figure 2.

To illustrate this geometric effect, we compare the effective regions involved in both approaches using a simple area-based construction. The excluded region in the disk-centered geometry is a circle centered on the observer with radius

$$R_{\text{excl}} = R_{\text{total}} - R_{\text{obs}}. \tag{4}$$

Thus, the effective contributing area is given by the total disk area minus the excluded region:

$$A_{\text{eff}} = \pi R_{\text{total}}^2 - \pi (R_{\text{total}} - R_{\text{obs}})^2. \tag{5}$$

Expanding this expression, we obtain:

$$A_{\text{eff}} = \pi \left(2R_{\text{total}}R_{\text{obs}} - R_{\text{obs}}^2\right) = \pi R_{\text{obs}} \left(2R_{\text{total}} - R_{\text{obs}}\right) \tag{6}$$

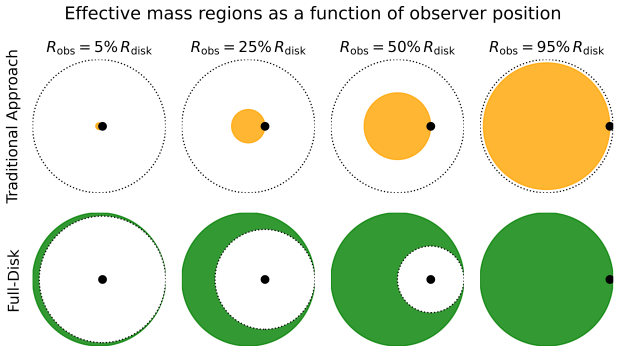

Figure 2: Comparison of the effective regions considered in the traditional approach (top, orange) and in the full-disk geometric construction (bottom, green) for different observer positions. In the latter, the excluded region is the largest disk centered on the observer that remains fully inside the galaxy, leaving a crescent-shaped region that contributes to the net gravitational field.

The ratio between the traditional and effective areas is therefore:

$$\frac{A_{\text{trad}}}{A_{\text{eff}}} = \frac{\pi R_{\text{obs}}^2}{\pi R_{\text{obs}}(2R_{\text{total}} - R_{\text{obs}})} = \frac{R_{\text{obs}}}{2R_{\text{total}} - R_{\text{obs}}}. \tag{7}$$

The behavior of this ratio is shown in Figure 3.

Near the galactic center, the region excluded by local symmetry occupies most of the disk, leaving only a thin crescent at the outer edge as the net contributing region. As the observer approaches the disk boundary, this excluded region shrinks and both approaches converge.

Although real galaxies do not exhibit uniform surface density, this simplified example highlights the geometric origin of the discrepancy. In realistic exponential disks, the same qualitative effect persists: neglecting external mass leads to an incomplete evaluation of the gravitational field.

3. The Lost and Found (LF) Model

3.1. Conceptual Framework

The analysis presented in Section 2 shows that the traditional enclosed-mass approximation introduces a geometric bias when applied to disk systems. This bias arises because mass elements located outside the observer's radius do not generally cancel in flattened geometries.

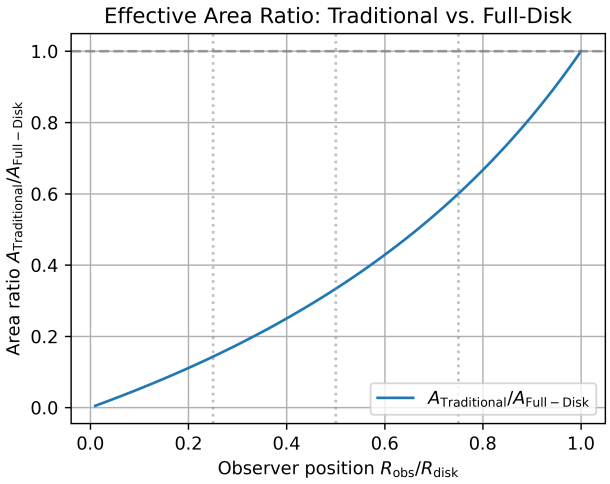

Figure 3: Ratio of effective areas considered by the traditional approach and the full-disk geometric construction as a function of observer radius. The traditional enclosed-mass approximation strongly underestimates the contributing region near the galactic center and approaches the full-disk effective area only near the disk edge.

Motivated by this observation, we introduce the *Lost and Found* (LF) model. The model combines a geometrically consistent evaluation of the gravitational field through full-disk integration with a two-component parametrization of the disk surface density, allowing both the global disk contribution and the radial mass structure to be treated self-consistently.

In this framework, the gravitational field at any point in the disk is determined by the superposition of contributions from all mass elements. Rather than assuming that only the enclosed mass contributes, the LF model consistently accounts for both interior and exterior regions of the disk. The surface density is represented here through a two-component exponential profile, allowing the model to capture both centrally concentrated and extended mass distributions.

3.2. Mathematical Formulation

We model the surface mass density of the galactic disk using a two-component exponential profile:

$$\Sigma(r) = \Sigma_1 e^{-r/r_1} + \Sigma_2 e^{-r/r_2}, \tag{8}$$

where Σ_1 and Σ_2 are the central surface densities of the inner and outer components, and r_1 and r_2 are their corresponding scale lengths.

This parametrization provides sufficient flexibility to represent a broad range of galactic mass distributions, including both centrally concentrated and extended disk structures. In particular, it accommodates deviations from a single exponential profile that are commonly observed in spiral galaxies [Freeman, 1970].

Rather than treating Σ_1 and Σ_2 as independent free amplitudes, the model is more conveniently expressed in terms of the total LF-inferred disk mass M_{LF} and a fractional mass parameter f, such that

$$M_1 = f\, M_{\mathrm{LF}}, \qquad M_2 = (1-f)\, M_{\mathrm{LF}}, \tag{9}$$

where M_1 and M_2 are the masses associated with the inner and outer exponential components, respectively. The corresponding central surface densities are then determined by normalization over the finite disk.

To represent a disk of finite extent while avoiding an artificial sharp edge, the total surface density is smoothly truncated near the outer radius of the model:

$$\Sigma(r) = \left[\Sigma_1 e^{-r/r_1} + \Sigma_2 e^{-r/r_2}\right] C(r), \tag{10}$$

where the tapering function is

$$C(r) = \frac{1}{1 + \exp\left(\frac{r - R_{\mathrm{cut}}}{\Delta}\right)}. \tag{11}$$

Here, R_{cut} is the truncation radius and Δ controls the smoothness of the transition. This tapering ensures that the disk mass remains finite and avoids numerical artifacts associated with a hard outer cutoff.

In the numerical implementation, the surface density is renormalized after the tapering is applied so that the total integrated mass of the final disk model remains equal to M_{LF}. Thus, M_{LF} corresponds to the total mass of the truncated model actually used in the gravitational calculation.

In practice, the truncation radius was not treated as an independent free parameter, but was fixed as a fraction of the fitted outer disk extent:

$$R_{\mathrm{cut}} = 0.95\, R_{\mathrm{max}}, \tag{12}$$

where R_{max} is the effective outer radius of the modeled disk. The free structural parameters of the LF model are therefore M_{LF}, f, r_1, r_2, and R_{max}.

The gravitational acceleration at a position $\vec{r}_{\mathrm{obs}}$ in the disk is computed as the vector sum of contributions from all mass elements:

$$\vec{a}(\vec{r}_{\mathrm{obs}}) = -G \iint_{\mathrm{disk}} \frac{\Sigma(r')\,(\vec{r}_{\mathrm{obs}} - \vec{r}')}{|\vec{r}_{\mathrm{obs}} - \vec{r}'|^3}\, d^2r'. \tag{13}$$

This expression makes no assumption of spherical symmetry and directly evaluates the gravitational

field generated by a continuous mass distribution in the plane of the disk.

The rotational velocity is then obtained from the radial component of the acceleration:

$$v(R) = \sqrt{R\, a_R(R)}, \tag{14}$$

where $a_R(R)$ denotes the inward radial component of the acceleration.

Unlike the traditional relation $v^2 = GM(< R)/R$, this formulation naturally includes the gravitational influence of both interior and exterior disk mass. In this sense, the LF model provides a direct Newtonian treatment of galactic disk gravity without recourse to spherical-equivalent approximations.

In the following section, we describe the numerical implementation used to evaluate this integral and to fit the resulting rotation curves to observational data.

4. Numerical Methodology

4.1. Disk Discretization

The gravitational integral is evaluated numerically by discretizing the galactic disk into concentric rings and angular sectors. The disk is divided into N_r radial bins and N_θ azimuthal bins, forming a two-dimensional grid in polar coordinates.

Each grid element, located at $\vec{r}' = (r', \theta')$, is assigned a surface density $\Sigma(r')$ and an area element

$$dA = r'\, dr'\, d\theta'. \tag{15}$$

The associated mass element is

$$dm_{i,j} = \Sigma(r'_i)\, r'_i\, \Delta r\, \Delta\theta. \tag{16}$$

After applying the smooth outer tapering, the surface density is renormalized so that the total integrated mass of the discretized disk remains equal to the fitted value $M_{\rm LF}$. The total LF-inferred mass is therefore recovered through

$$M_{\rm LF} = \sum_{i,j} dm_{i,j}. \tag{17}$$

4.2. Acceleration Calculation

The gravitational acceleration at a given observer position $R_{\rm obs}$ is computed as

$$\vec{a}(R_{\rm obs}) = -G \sum_{i,j} \frac{dm_{i,j}\,(\vec{r}_{\rm obs} - \vec{r}'_{i,j})}{|\vec{r}_{\rm obs} - \vec{r}'_{i,j}|^3}. \tag{18}$$

The radial component $a_R(R)$ is obtained by projection, where $a_R(R)$ denotes the inward radial acceleration. The rotation velocity then follows as

$$v(R) = \sqrt{R\, a_R(R)}. \tag{19}$$

To avoid numerical divergences when the observer position approaches a grid cell, a softening term ϵ is introduced:

$$|\vec{r}_{\rm obs} - \vec{r}'|^2 \to |\vec{r}_{\rm obs} - \vec{r}'|^2 + \epsilon^2. \tag{20}$$

This regularization preserves the large-scale gravitational behavior while preventing singular contributions.

4.3. Parameter Optimization

The LF model was fitted to observed rotation curves by optimizing the parameters $(M_{\rm LF}, f, r_1, r_2, R_{\rm max})$.

For each parameter set, the model rotation curve was computed and interpolated to the observed radii. The fit quality was quantified using a weighted chi-square statistic when observational uncertainties were available,

$$\chi^2 = \sum_k \frac{[v_{\rm obs}(R_k) - v_{\rm model}(R_k)]^2}{\sigma_k^2}, \tag{21}$$

and by the unweighted sum of squared residuals otherwise.

The optimization was performed in two stages. First, an adaptive grid of $M_{\rm LF}$ values was constructed around an initial dynamical estimate. For each trial mass, the remaining parameters were optimized using the derivative-free Nelder–Mead simplex algorithm [Nelder and Mead, 1965, Lagarias et al., 1998], which is well suited for nonlinear problems involving multiple coupled parameters. A second, finer scan around the best solution was then used to refine the optimum and estimate uncertainties using the criterion

$$\Delta\chi^2 \leq 1. \tag{22}$$

This hybrid approach improves robustness against local minima and ensures stable convergence across galaxies with different morphologies.

4.4. Validation Tests

Validation checks using simplified mass distributions confirmed that the numerical implementation behaves as expected in idealized configurations. In particular, for approximately uniform inner density profiles, the

resulting rotation curves show the expected near-linear rise in the central region, consistent with solid-body-like behavior.

At larger radii, the contribution of extended disk mass naturally modifies the outer rotational behavior and can produce a progressive flattening of the rotation curve, depending on the adopted surface density profile.

Convergence tests show that the results become stable beyond a certain resolution threshold. Typical simulations used $N_r \sim 200$ and $N_\theta \sim 400$, providing a balance between accuracy and computational cost.

5. Results

5.1. Galaxy Sample

The LF model was applied to a heterogeneous sample of spiral galaxies with high-quality rotation curve data. The full list of galaxies analyzed is provided in Table 1.

The sample includes both classical systems extensively studied in the literature, particularly in Begeman et al. [1991], as well as additional galaxies drawn from more recent compilations such as the SPARC database [Lelli et al., 2016], which assembles high-quality rotation curves and associated photometric and H I measurements from the original observational literature. This combined dataset spans a wide range of masses, surface brightness profiles, and rotation curve morphologies, allowing us to test the robustness and general applicability of the LF model across different galactic environments.

For M33, which is not included in the SPARC database, the baryonic mass was adopted from the literature using representative values for the stellar and gas components. We use

$$M_{\rm bar} \approx 8.0 \times 10^9\, M_\odot, \tag{23}$$

consistent with studies of the baryonic distribution and gas content of M33 [Corbelli et al., 2014, Gratier et al., 2017, Corbelli, 2003].

5.2. Rotation Curves Across the Sample

Figures 4 and 5 show the observed rotation curves and the corresponding LF model fits for the galaxy sample, ordered approximately by increasing radial extent. Observed velocities are shown as points with uncertainties, while the LF best-fit curves are shown as solid lines.

Across the sample, the LF model reproduces the main features of the observed rotation curves, including the inner rising regions and, where present, the transition toward flatter outer behavior. The agreement is observed over a broad range of galaxy sizes and kinematic morphologies.

When the galaxies are ordered by increasing $R_{\rm max}$, a systematic morphological progression becomes apparent. The smallest systems are dominated by a nearly linear inner rise, whereas progressively larger systems reveal increasing curvature, turnover, and extended flatter outer regions. This trend suggests a systematic variation in rotation-curve morphology with increasing radial extent.

5.3. Fit Quality

The quality of the fits was quantified using the coefficient of determination (R^2), the root-mean-square (RMS) residual, and the reduced chi-square when observational uncertainties were available:

$$\mathrm{RMS} = \sqrt{\frac{1}{N}\sum_i \left(v_{\mathrm{obs},i} - v_{\mathrm{model},i}\right)^2}, \tag{24}$$

$$R^2 = 1 - \frac{\sum_i \left(v_{\mathrm{obs},i} - v_{\mathrm{model},i}\right)^2}{\sum_i \left(v_{\mathrm{obs},i} - \bar{v}_{\mathrm{obs}}\right)^2}, \tag{25}$$

$$\chi^2_\nu = \frac{1}{N-p}\sum_i \left(\frac{v_{\mathrm{obs},i} - v_{\mathrm{model},i}}{\sigma_i}\right)^2, \tag{26}$$

where N is the number of observed data points, p is the number of free parameters, and σ_i are the observational velocity uncertainties.

For most galaxies in the sample, the LF model achieves values of R^2 close to unity, indicating excellent agreement with the observed rotation curves. Several galaxies, such as NGC 3198, NGC 0024, and UGC 02259, show $R^2 > 0.99$. The RMS residuals are typically of the order of a few $\mathrm{km\,s^{-1}}$, indicating that the deviations between model and observations remain small in absolute terms.

A small number of galaxies exhibit lower or even formally negative R^2 values despite visually reasonable fits. This occurs when the observed velocity profile contains strong local fluctuations or large point-to-point scatter, especially in the inner regions, making R^2 overly sensitive to deviations relative to the sample mean. In such cases, the RMS residual and the reduced chi-square, when available, provide more robust indicators of fit quality than R^2 alone.

While R^2 provides a convenient measure of visual agreement, χ^2_ν is more physically meaningful because it incorporates the observational uncertainties. In

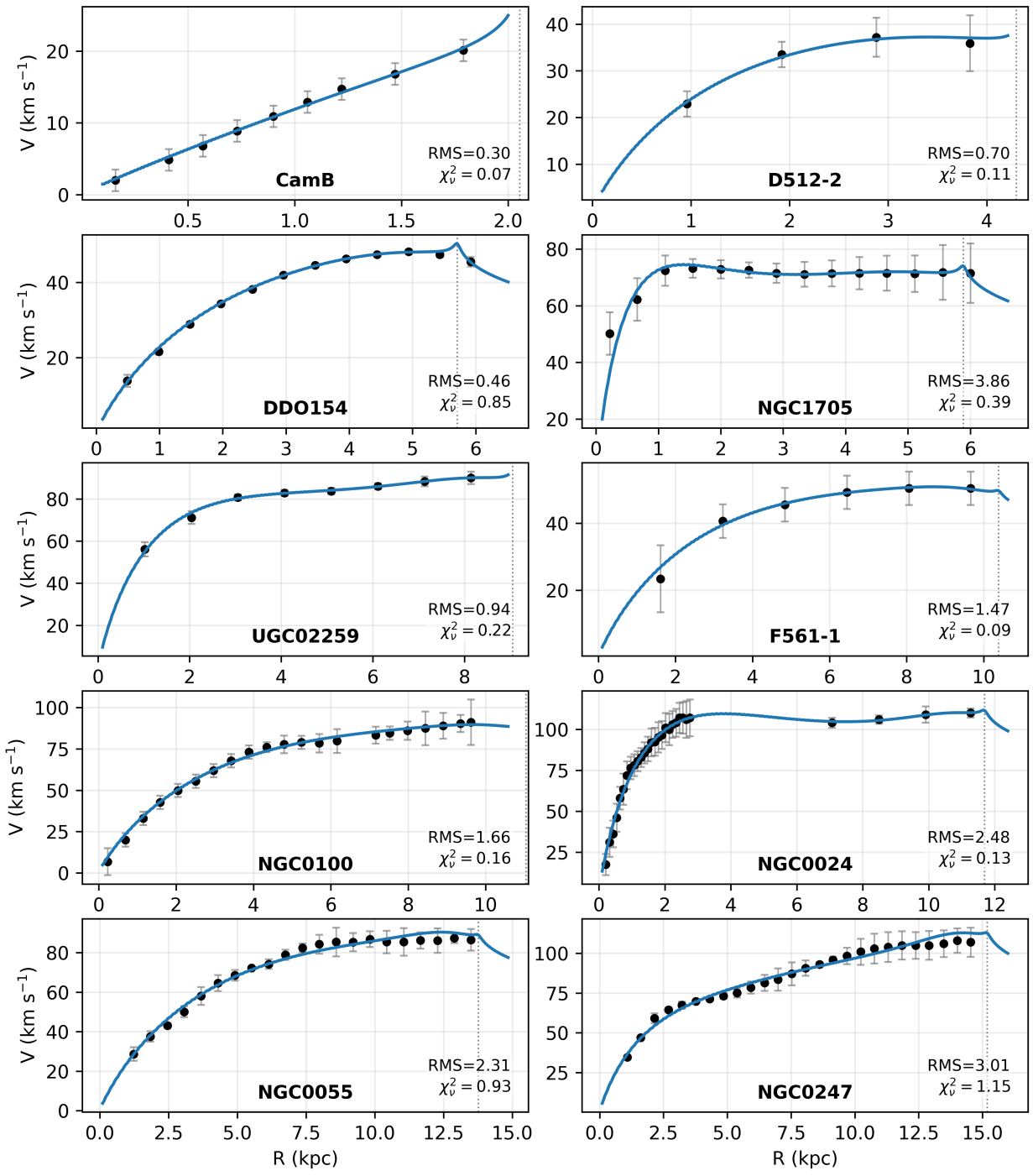

Figure 4: Rotation curves for the small- and intermediate-size galaxies in the sample. Observed velocities (points with error bars) are compared with the LF model best-fit curves (solid lines). The galaxies are ordered approximately by increasing radial extent.

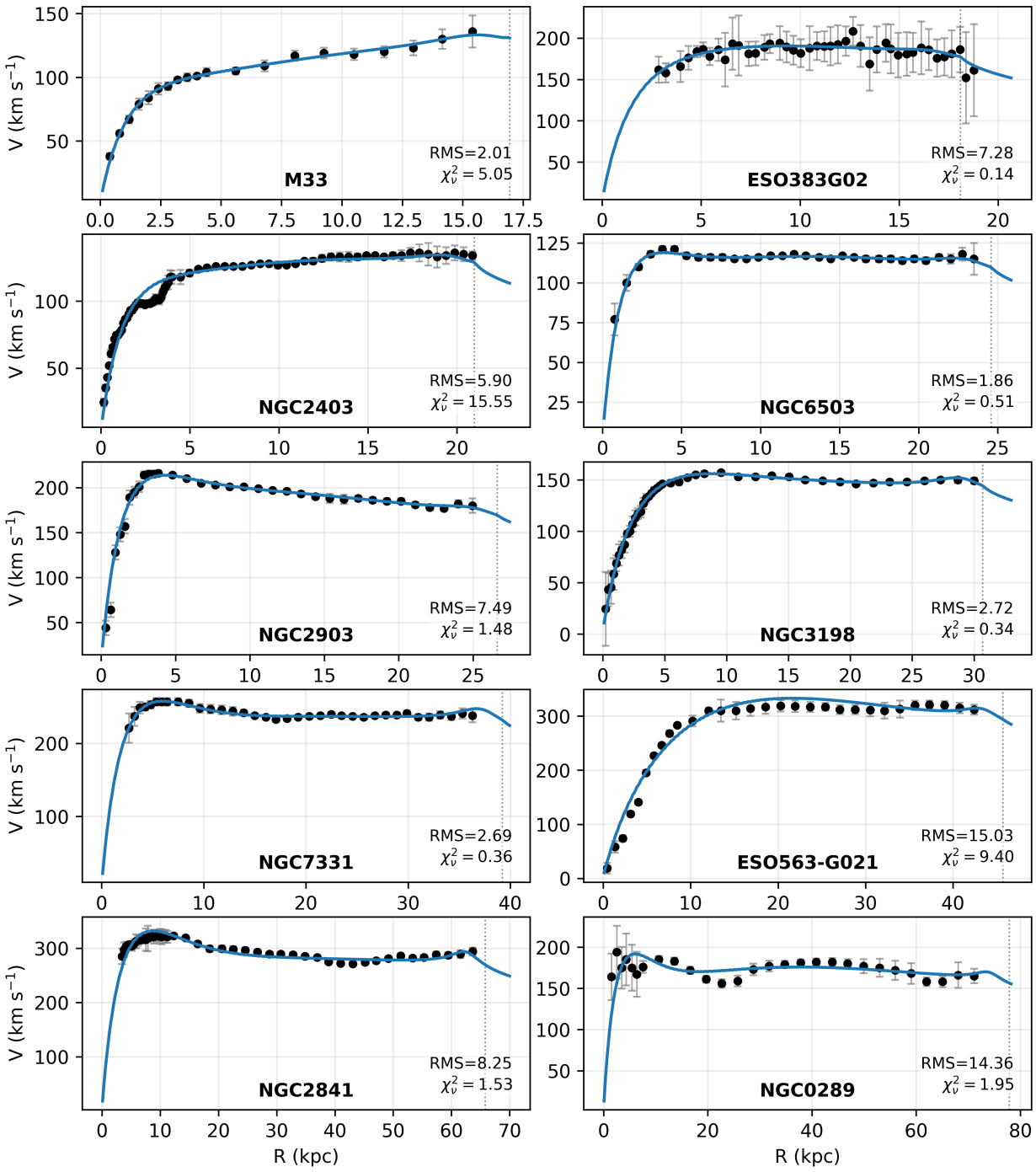

Figure 5: Rotation curves for the largest galaxies in the sample. Observed velocities (points with error bars) are compared with the LF model best-fit curves (solid lines). The galaxies are ordered approximately by increasing radial extent.

this sense, some galaxies with modest or even negative R^2 values still exhibit statistically acceptable fits, while others with visually smooth agreement may yield larger χ^2_ν due to small error bars or localized fluctuations in the observed rotation curve.

5.4. Radial Extent Comparison

A useful consistency test is provided by comparing the LF parameter $R_{\rm max}$ with the maximum observed radial extent of the rotation curve, $R^{\rm obs}_{\rm max}$, obtained directly from the kinematic data.

We find that these quantities are generally in close agreement:

$$\frac{R_{\rm max}}{R^{\rm obs}_{\rm max}} \approx 1, \tag{27}$$

with deviations typically within about 10%.

This result indicates that the LF model naturally recovers the observed radial extent of the disks without requiring external tuning. It also suggests that the relevant radial scale in the LF framework is not simply the photometric exponential scale length often quoted in the literature, but rather the full observed kinematic extent of the system.

5.5. Mass Comparison

A central question in any rotation-curve analysis is how the mass required to reproduce the observed kinematics compares with both the observed baryonic content and the dynamical mass conventionally inferred from the outer rotation speed. This comparison is particularly relevant in the context of the long-standing discrepancy between luminous matter and rotation-curve amplitudes reported in disk galaxies Rubin et al. [1980], Bosma [1981], Begeman et al. [1991], Sofue and Rubin [2001], de Blok et al. [2008], Lelli et al. [2016].

To evaluate the LF model in this context, we compared the LF-inferred mass $M_{\rm LF}$ with two independent reference masses.

First, the baryonic mass was estimated from stellar and gas components as

$$M_{\rm bar} = \Upsilon_* L_{[3.6]} + 1.33\, M_{\rm HI}, \tag{28}$$

where $\Upsilon_* = 0.5$ was adopted for the stellar mass-to-light ratio in the 3.6 μm band, following the standard assumptions used in SPARC-based analyses Lelli et al. [2016], McGaugh et al. [2016].

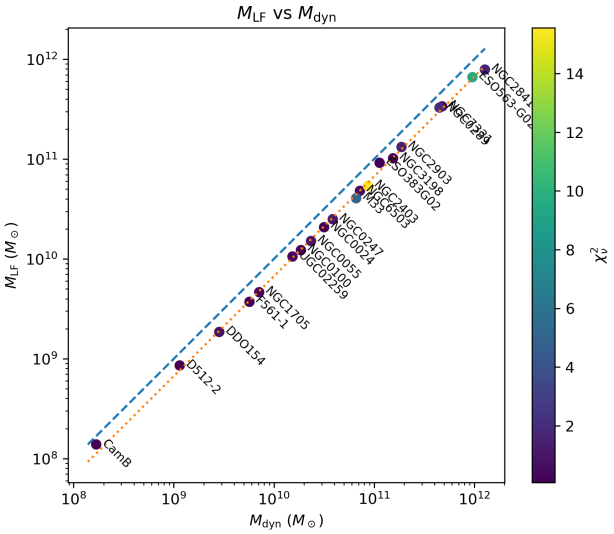

Figure 6: Comparison between the LF-inferred mass and the dynamical mass inferred at the outermost observed point of the rotation curve. The dashed line indicates the one-to-one relation, while the dotted line shows the global proportionality trend. Points are color-coded by reduced chi-square.

Second, the dynamical mass was estimated at the outermost observed point of each rotation curve as

$$M_{\rm dyn}(R^{\rm obs}_{\rm max}) = \frac{v(R^{\rm obs}_{\rm max})^2\, R^{\rm obs}_{\rm max}}{G}, \tag{29}$$

where $v(R^{\rm obs}_{\rm max})$ is the observed rotation velocity at the largest measured radius. This quantity represents the standard spherical-equivalent dynamical mass enclosed within the observed extent of the rotation curve. It should be distinguished from virial halo masses or model-dependent dark matter halo masses often quoted in the literature, which generally refer to larger extrapolated scales.

Figure 6 compares the LF-inferred mass with the dynamical mass. A stable relation is found across the sample. Using the total masses, we obtain

$$\frac{\sum M_{\rm LF}}{\sum M_{\rm dyn}} = 0.671, \tag{30}$$

while the average of galaxy-by-galaxy ratios yields

$$\left\langle \frac{M_{\rm LF}}{M_{\rm dyn}} \right\rangle = 0.681 \pm 0.013, \tag{31}$$

with a standard deviation of 0.058 and a median value of 0.658.

A linear fit constrained through the origin gives

$$M_{\rm LF} = 0.654\, M_{\rm dyn}, \tag{32}$$

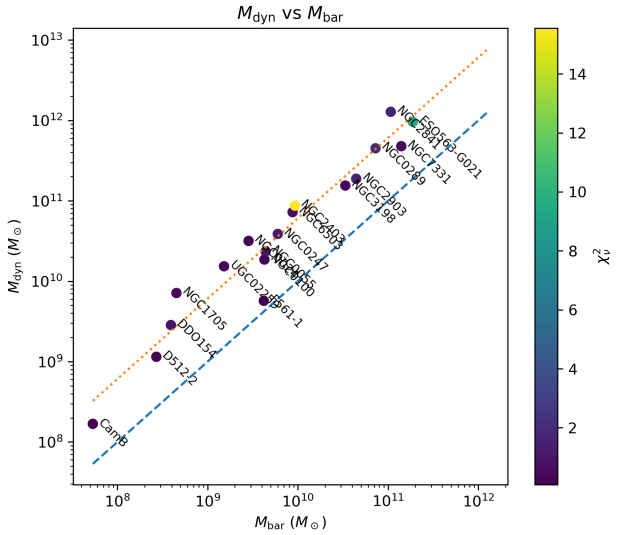

Figure 7: Comparison between the dynamical mass and the baryonic mass. The dashed line indicates the one-to-one relation, while the dotted line shows the global proportionality trend. Points are color-coded by reduced chi-square.

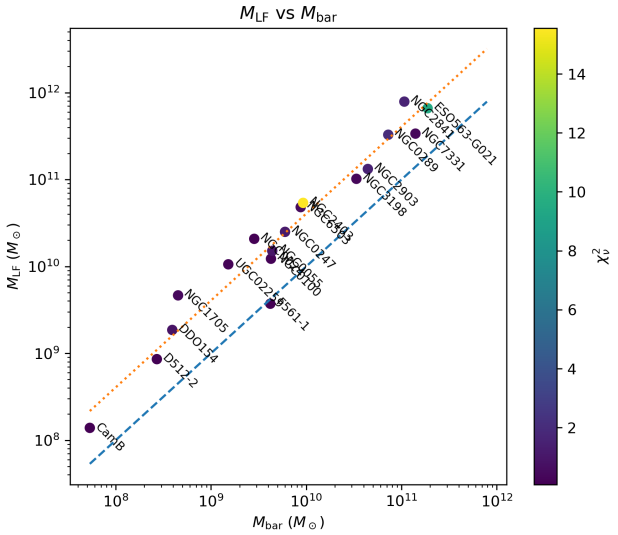

Figure 8: Comparison between the LF-inferred mass and the baryonic mass estimated from stellar and H I data. The dashed line indicates the one-to-one relation, while the dotted line shows the global proportionality trend. Points are color-coded by reduced chi-square.

while the logarithmic fit yields

$$\log M_{\rm LF} = 0.989\, \log M_{\rm dyn} - 0.054, \tag{33}$$

or equivalently,

$$M_{\rm LF} \approx 0.883\, M_{\rm dyn}^{0.989}. \tag{34}$$

The logarithmic slope, being very close to unity, indicates that the LF-inferred mass scales almost linearly with the dynamical mass over the full sample. Thus, the main difference between the two quantities is not a change in scaling with galaxy mass, but rather a systematic offset in normalization.

To express this trend more compactly, we define the LF mass reduction factor as

$$\eta_{\rm LF} \equiv \frac{M_{\rm LF}}{M_{\rm dyn}}, \tag{35}$$

where $M_{\rm LF}$ is the LF-inferred mass and $M_{\rm dyn}$ is the standard dynamical mass estimate. Across the galaxy sample analyzed here, this ratio clusters around

$$\eta_{\rm LF} \sim 0.67. \tag{36}$$

Figure 7 compares the dynamical mass with the baryonic mass. As expected from classical rotation-curve studies, the dynamical mass lies well above the directly estimated baryonic content for most galaxies.

Using the total masses, we obtain

$$\frac{\sum M_{\rm dyn}}{\sum M_{\rm bar}} = 6.075, \tag{37}$$

while the galaxy-by-galaxy average gives

$$\left\langle \frac{M_{\rm dyn}}{M_{\rm bar}} \right\rangle = 6.80 \pm 0.87, \tag{38}$$

with a standard deviation of 3.68 and a median value of 5.77.

A linear fit constrained through the origin gives

$$M_{\rm dyn} = 5.77\, M_{\rm bar}, \tag{39}$$

while the logarithmic fit yields

$$\log M_{\rm dyn} = 0.995\, \log M_{\rm bar} + 0.821, \tag{40}$$

or equivalently,

$$M_{\rm dyn} \approx 6.63\, M_{\rm bar}^{0.995}. \tag{41}$$

The near-unity logarithmic slope indicates that the conventional dynamical mass also scales almost linearly with baryonic mass across the sample, but with a substantially larger normalization than the LF relation discussed above.

Figure 8 compares the LF-inferred mass with the baryonic mass. In contrast to the comparison with $M_{\rm dyn}$, the LF-inferred mass systematically exceeds the baryonic estimate, although by a smaller factor than the standard dynamical mass does. Using the ratio of total masses, we find

$$\frac{\sum M_{\rm LF}}{\sum M_{\rm bar}} = 4.05, \tag{42}$$

while the average galaxy-by-galaxy ratio is

$$\left\langle \frac{M_{\rm LF}}{M_{\rm bar}} \right\rangle = 4.53 \pm 0.54, \tag{43}$$

with a standard deviation of 2.31 and a median value of 3.85.

A linear fit constrained through the origin gives

$$M_{\rm LF} = 3.87\, M_{\rm bar}, \tag{44}$$

while the logarithmic fit yields

$$\log M_{\rm LF} = 0.985\, \log M_{\rm bar} + 0.748, \tag{45}$$

or equivalently,

$$M_{\rm LF} \approx 5.60\, M_{\rm bar}^{0.985}. \tag{46}$$

The logarithmic slope remains close to unity, suggesting that the LF-inferred mass broadly follows the baryonic mass scaling across the sample, albeit with substantially larger scatter than in the comparison with $M_{\rm dyn}$. This larger scatter is expected, as baryonic mass estimates are subject to additional systematic uncertainties, including stellar mass-to-light ratios and gas mass determinations.

Taken together, these comparisons show that the LF model occupies an intermediate scaling between the observed baryonic mass and the conventional dynamical mass. The required LF mass is systematically larger than the directly observed baryonic content, but also systematically smaller than the dynamical mass inferred from the outer rotation velocity. This intermediate scaling is one of the most consistent empirical signatures of the model across the present galaxy sample.

An especially notable case is F561-1, for which the LF-inferred mass is nearly consistent with the estimated baryonic mass.

5.6. Best-Fit Parameters

Table 1 summarizes the fitted structural parameters of the LF model for the galaxy sample, together with the corresponding baryonic and dynamical reference masses.

The fitted parameters show a consistent two-scale behavior, with an inner component characterized by a shorter radial scale and an outer component extending to larger radii. This pattern reflects the requirement to reproduce both the steep inner rise and the extended outer regions of the observed rotation curves.

The parameter f, which controls the fraction of the total LF-inferred mass assigned to the inner exponential component, varies substantially across the sample, indicating that the LF model does not impose a universal fixed partition between inner and outer structure. Instead, the relative contribution of both components adapts naturally to the observed kinematic profile of each galaxy.

6. Discussion

6.1. Geometric Interpretation of the LF Correction

The results obtained with the LF framework indicate that a substantial part of the observed rotation-curve behavior, including the tendency toward outer flattening, can arise from the geometry of the disk itself when the full gravitational contribution of the mass distribution is taken into account.

In conventional analyses, the gravitational field is often approximated using the spherical relation

$$v^2(R) = \frac{GM(<R)}{R}, \tag{47}$$

which is exact only under spherical symmetry [Binney and Tremaine, 2011]. For flattened systems, however, this approximation neglects the contribution of mass exterior to the radius of interest. The LF model shows that when the gravitational field is evaluated through direct integration of the full disk, the outer mass continues to contribute significantly to the acceleration at interior radii [Freeman, 1970, Casertano, 1983].

As a result, the same observed rotation curves can be reproduced with systematically smaller masses than those inferred from spherical-equivalent estimates. Across the present sample, this manifests as a nearly constant mass reduction factor $\eta_{\rm LF} \sim 0.67$. This suggests that part of the inferred mass discrepancy in disk galaxies may reflect the geometric assumptions underlying standard mass inference, rather than exclusively the presence of additional mass components.

Table 1: Summary of LF model fitted parameters. Here, N is the number of observed rotation-curve points; $M_{\rm LF}$ is the total LF-inferred mass; $M_{\rm bar}$ is the baryonic mass; $M_{\rm dyn}$ is the dynamical mass estimated at the outermost observed radius; f is the mass fraction of the inner component ($M_1 = f\,M_{\rm LF}$); r_1 and r_2 are the scale lengths of the inner and outer exponential components; $R_{\rm max}^{\rm obs}$ is the maximum observed radius; $R_{\rm max}$ is the best-fit truncation radius; $v(R_{\rm max}^{\rm obs})$ is the observed velocity at the outermost point; and χ^2_ν is the reduced chi-square of the fit. For galaxies not included in the SPARC sample, baryonic masses were adopted from available literature estimates when possible. Entries left blank indicate cases for which a consistent baryonic mass estimate was not included in the present comparison.

Galaxy	N	$M_{\rm LF}$ ($M_\odot$)	$M_{\rm bar}$ ($M_\odot$)	$M_{\rm dyn}$ ($M_\odot$)	f	r_1 (kpc)	r_2 (kpc)	$R_{\rm max}^{\rm obs}$ (kpc)	$R_{\rm max}$ (kpc)	$v(R_{\rm max}^{\rm obs})$ (km/s)	χ^2_ν
CamB	9	1.39×10^{8}	5.35×10^{7}	1.68×10^{8}	0.010	15.00	29.42	1.79	2.05	20.1	0.071
D512-2	4	8.57×10^{8}	2.70×10^{8}	1.15×10^{9}	0.959	1.69	6.30	3.83	4.30	35.9	0.106
DDO154	12	1.86×10^{9}	3.92×10^{8}	2.85×10^{9}	0.972	2.60	20.10	5.92	5.71	45.5	0.848
NGC1705	14	4.64×10^{9}	4.51×10^{8}	7.13×10^{9}	0.720	3.10	0.50	6.00	5.89	71.5	0.388
F561-1	6	3.72×10^{9}	4.20×10^{9}	5.71×10^{9}	0.985	3.52	3.89	9.66	10.39	50.4	0.087
UGC02259	8	1.06×10^{10}	1.52×10^{9}	1.53×10^{10}	0.309	1.27	6.03	8.14	9.05	90.0	0.219
NGC0100	21	1.23×10^{10}	4.26×10^{9}	1.86×10^{10}	0.962	3.90	60.00	9.62	11.04	91.2	0.160
NGC0024	29	2.08×10^{10}	2.84×10^{9}	3.17×10^{10}	0.406	1.41	9.23	11.27	11.69	110	0.129
NGC0055	21	1.51×10^{10}	4.40×10^{9}	2.35×10^{10}	0.066	5.33	5.33	13.50	13.76	86.5	0.929
NGC0247	26	2.50×10^{10}	5.99×10^{9}	3.87×10^{10}	0.075	1.66	8.27	14.54	15.18	107	1.153
M33	20	4.06×10^{10}	8.00×10^{9}	6.62×10^{10}	0.102	1.21	7.34	15.40	16.94	136	5.048
ESO383G02	42	9.19×10^{10}	—	1.14×10^{11}	0.847	5.36	1.59	18.78	18.09	161	0.136
NGC2403	73	5.39×10^{10}	9.28×10^{9}	8.71×10^{10}	0.128	1.34	6.92	20.87	20.97	134	15.553
NGC6503	31	4.81×10^{10}	8.74×10^{9}	7.23×10^{10}	0.177	1.24	7.44	23.50	24.58	115	0.507
NGC2903	34	1.32×10^{11}	4.43×10^{10}	1.88×10^{11}	0.252	1.46	7.22	24.96	26.62	180	1.479
NGC3198	43	1.02×10^{11}	3.36×10^{10}	1.55×10^{11}	0.297	2.79	11.62	30.00	30.69	149	0.341
NGC7331	36	3.37×10^{11}	1.40×10^{11}	4.78×10^{11}	0.221	2.15	13.77	36.31	39.21	238	0.363
ESO563-G021	30	6.62×10^{11}	1.88×10^{11}	9.60×10^{11}	0.865	9.42	60.00	42.41	45.69	312	9.403
NGC2841	50	7.88×10^{11}	1.07×10^{11}	1.28×10^{12}	0.262	3.38	22.96	63.64	65.80	294	1.530
NGC0289	28	3.28×10^{11}	7.26×10^{10}	4.50×10^{11}	0.148	2.25	20.61	71.12	77.86	165	1.951

6.2. Relation to Baryonic Mass and Residual Discrepancy

Although the LF model reduces the discrepancy relative to $M_{\rm dyn}$, the LF-inferred mass remains systematically larger than the estimated baryonic mass. This residual difference can arise from several sources.

Baryonic mass estimates depend on photometric light profiles, H I measurements, and assumptions about mass-to-light ratios, gas corrections, and low-surface-brightness outskirts [de Blok et al., 2008, Lelli et al., 2016]. These factors introduce uncertainties that may lead to an underestimation of the total effective gravitating disk mass.

In addition, the LF surface density profile is an effective parametrization. The fitted mass distribution may also absorb part of the contribution from extended or diffuse structures that are not always fully captured in simplified photometric decompositions.

The position of $M_{\rm LF}$ between $M_{\rm bar}$ and $M_{\rm dyn}$ therefore suggests that geometric effects can account for a significant fraction of the inferred discrepancy, even if a residual mass excess remains to be explained [McGaugh et al., 2016].

6.3. Interpretive Scope of the LF Model

The LF framework does not introduce new mass components or modify Newtonian gravity. Instead, it revisits how the gravitational field is computed in flattened systems. In this sense, it is distinct from both dark matter halo models and modified-gravity approaches such as MOND.

The LF-inferred surface density should be interpreted as an effective gravitating distribution rather than a unique reconstruction of the physical baryonic mass. The adopted two-component exponential profile provides a simplified effective description of the radial mass distribution, but does not capture the full structural complexity of real galaxies.

Accordingly, the present results should be understood as demonstrating the impact of geometric treatment on mass inference, rather than as a definitive decomposition of the underlying baryonic structure.

6.4. Observational and Modeling Limitations

Several limitations of the present analysis should be noted.

First, the use of a two-component exponential profile is a simplified representation of the disk structure. While it reproduces a wide range of rotation-curve morphologies, it is not intended as a unique or fully realistic description of the stellar and gaseous mass distribution.

Second, the model assumes an axisymmetric thin disk. Non-axisymmetric features such as bars, spiral arms, and local asymmetries are not explicitly included.

Third, the baryonic comparison is limited by the availability and consistency of observational data.

Finally, the dynamical mass $M_{\rm dyn}$ used for comparison is a spherical-equivalent estimate at the outermost observed radius.

6.5. Implications and Future Directions

The results presented here motivate several directions for further investigation.

Applying the LF framework to larger and more homogeneous galaxy samples will be essential to assess the robustness of the mass reduction factor across different galaxy types.

A particularly important step will be to replace the present effective mass profiles with surface density distributions directly constrained from observed stellar and gas maps.

These extensions will help determine how much of the apparent mass discrepancy can be accounted for by geometry alone, and how much may still require additional physical ingredients.

7. Conclusions

We have shown that a geometrically consistent Newtonian treatment of flattened disk systems can reproduce the main observed features of galactic rotation curves while systematically reducing the total mass required relative to conventional spherical-equivalent estimates.

Across the present sample, the LF framework yields a characteristic mass reduction factor $\eta_{\rm LF} \sim 0.67$, suggesting that part of the inferred mass discrepancy in disk galaxies may arise from geometric assumptions in standard mass inference. Although the LF-inferred mass generally remains larger than the directly estimated baryonic mass, the results indicate that geometry alone can account for a substantial fraction of the discrepancy.

These findings motivate a reassessment of how gravitational fields are evaluated in non-spherical systems, and call for future tests of the LF framework using directly observed stellar and gas surface density profiles.

Acknowledgements

The author gratefully acknowledges the academic environment and institutional support provided by the University of New Hampshire, which helped make this work possible. Work at the University of New Hampshire is supported by NASA grants 80NSSC24K1245, 80NSSC21K0463, and 80NSSC23K1057. This research was developed independently and outside the primary scientific scope of those funded activities.

This work made use of the SPARC database [Lelli et al., 2016]. The author further acknowledges the original observational studies compiled therein, whose high-quality rotation-curve and photometric data form an essential foundation for the present analysis.

Data Availability

The data underlying this article are publicly available from the SPARC database [Lelli et al., 2016], accessible at `http://astroweb.cwru.edu/SPARC/`, together with a small number of additional literature sources cited explicitly in the text. The numerical outputs and derived data products generated in this work are available from the author upon reasonable request.

A. Optional Appendix Title

References

K. G. Begeman, A. H. Broeils, and R. H. Sanders. Extended rotation curves of spiral galaxies: dark haloes and modified dynamics. *Monthly Notices of the Royal Astronomical Society*, 249:523–537, 1991.

James Binney and Scott Tremaine. *Galactic dynamics*. Princeton university press, 2011.

A. Bosma. 21-cm line studies of spiral galaxies. i. observations of the galaxies ngc 3198 and ngc 2403. *AJ*, 86:1825–1846, 1981. doi: 10.1086/113062.

Andreas Burkert. The structure of dark matter halos in dwarf galaxies. *The Astrophysical Journal*, 447 (1):L25, 1995.

S. Casertano. Rotation curve of the edge-on spiral galaxy ngc 5907: Disk and halo masses. *Monthly Notices of the Royal Astronomical Society*, 203:735–747, 1983.

E. Corbelli. Dark matter and visible baryons in m33. *Monthly Notices of the Royal Astronomical Society*, 342(1):199–207, 2003. doi: 10.1046/j.1365-8711.2003.06531.x.

E. Corbelli, D. Thilker, S. Zibetti, C. Giovanardi, and P. Salucci. Dynamical signatures of a λcdm-halo and the distribution of the baryons in m33. *Astronomy & Astrophysics*, 572:A23, 2014. doi: 10.1051/0004-6361/201424033.

W. J. G. de Blok, F. Walter, E. Brinks, C. Trachternach, S.-H. Oh, and R. C. Kennicutt. High-resolution rotation curves and galaxy mass models from things. *The Astronomical Journal*, 136(6):2648–2719, 2008. doi: 10.1088/0004-6256/136/6/2648.

James Q. Feng and C. F. Gallo. Mass distribution in rotating thin-disk galaxies according to newtonian dynamics. *Galaxies*, 1(2):79–101, 2013. doi: 10.3390/galaxies1020079. arXiv:1212.5317.

K.C. Freeman. On the disks of spiral and s0 galaxies. *The Astrophysical Journal*, 160:811, 1970.

P. Gratier, J. Braine, K. Schuster, and et al. The molecular gas mass of m33. *Astronomy & Astrophysics*, 600:A27, 2017. doi: 10.1051/0004-6361/201629300.

J. C. Lagarias, J. A. Reeds, M. H. Wright, and P. E. Wright. Convergence properties of the nelder–mead simplex method in low dimensions. *SIAM Journal on Optimization*, 9(1):112–147, 1998. doi: 10.1137/S1052623496303470.

Federico Lelli, Stacy S. McGaugh, and James M. Schombert. Sparc: Mass models for 175 disk galaxies with spitzer photometry and accurate rotation curves. *The Astronomical Journal*, 152(6):157, 2016. doi: 10.3847/0004-6256/152/6/157.

Stacy S. McGaugh, Federico Lelli, and James M. Schombert. Radial acceleration relation in rotationally supported galaxies. *Physical Review Letters*, 117(20):201101, 2016.

Mordehai Milgrom. A modification of the newtonian dynamics as a possible alternative to the hidden mass hypothesis. *The Astrophysical Journal*, 270:365–370, 1983.

Julio F Navarro. The structure of cold dark matter halos. In *Symposium-international astronomical union*, volume 171, pages 255–258. Cambridge University Press, 1996.

J. A. Nelder and R. Mead. A simplex method for function minimization. *The Computer Journal*, 7 (4):308–313, 1965. doi: 10.1093/comjnl/7.4.308.

Isaac Newton. *Philosophiae Naturalis Principia Mathematica*. Royal Society, 1687. Traducción de la edición original latina.

Vera C Rubin, W Kent Ford Jr, and Norbert Thonnard. Rotational properties of 21 sc galaxies with a large range of luminosities and radii, from ngc 4605/r= 4kpc/to ugc 2885/r= 122 kpc. *Astrophysical Journal, Part 1, vol. 238, June 1, 1980, p. 471-487.*, 238:471–487, 1980.

N. Ryan. Galactic disc rotation: Analytic models and asymptotic behavior. *J. Phys. A: Math. Theor.*, 46:225501, 2013. doi: 10.1088/1751-8113/46/22/225501. arXiv:1301.5233.

Yoshiaki Sofue and Vera Rubin. Rotation curves of spiral galaxies. *Annual Review of Astronomy and Astrophysics*, 39:137–174, 2001.